기초과학연구

목 차

통계학

TAYLOR'S POWER LAW FOR MIXED MODELS IN THE SEQUENTIAL SAMPLING·····1

HEUNGSUN PARK

수학

AN EXPLICIT FORMULATION OF THE LEARNED NOISE PREDICTOR ϵθ(xt, t) VIA THE FORWARD-PROCESS NOISE ϵt IN DENOISING DIFFUSION PROBABILISTIC MODELS (DDPMS)·····8

KIHYUN YUN

생명공학

Bacteriophage Therapy in Industry: A New Horizon in Antibacterial Treatment·····15

Heejoon Myung

Screening of potential immunosuppressive compounds that inhibit transcriptional activity of the Nuclear Factor of Activated T cell·····20

Jungchan park

전자물리학

Decoupling Doping Magnitude and Uniformity in Photoexcited WSe2/BN Heterostructures·····26

Taekyeong Kim

J. Basic Sci. HUFS **60** (2025), pp. 1-7

TAYLOR'S POWER LAW FOR MIXED MODELS IN THE SEQUENTIAL SAMPLING[1]

HEUNGSUN PARK*

Abstract. Taylor's Power Law has been widely used for describing the aggregation pattern for animals, insects or even social/economic phenomena. Park and Cho (2004) introduced the statistical modeling method to estimate the two parameters in Taylor's Power Law for the independent observations. In this, their study is expanded to cover the correlated observations including panel data. The suggested estimates are used to develop the stopping line in a sequential sampling scheme.

1. Taylor's Power Law

Taylor's Power Law is an empirical statistical relationship, originally discovered in ecology, that relates the variance of a population or process to its mean through a power-law function. Specifically, for a population count Y with mean μ and variance Var(Y), Taylor's Power Law is expressed as:

$$\mathrm{Var(Y)} = a\,\mu^b \tag{1}$$

or, equivalently,

$$\log(\mathrm{Var(Y)}) = \log(a) + b\,\log(\mu),\ (a > 0) \tag{2}$$

where a and b are positive constants. The exponent b is often interpreted as an index of aggregation or clustering in the population, with higher values indicating greater aggregation (Taylor 1961; Xu 2015)

Lionel Roy Taylor (1914-2007), a British ecologist, published an article entitled "Aggregation, variance and the mean" in the March 4, 1961 issue of Nature. In the paper, Taylor studied the relationship between the mean and the variance of population density for at least 22 biological species in 24 data sets (Xu 2015)

[1] This work was supported by Hankuk University of Foreign Studies Research Fund of 2024.

* Professor, Dept. of Statistics, Hankuk University of Foreign Studies, Yongin-si, Gyeonggi-do, South Korea. hspark@hufs.ac.kr .

Even though Taylor's Power Law (TPL) was first developed for studying insect population aggregation pattern, it has been confirmed for hundreds of species and other fields such as in ecology, epidemiology, genetics, economics, seismology, number theory and earthquake studies (Cohen 2016, Shi *et. al.* 2019, Cohen and Xu 2015)

If $b = 1$, the variance is proportional to the mean (as in a Poisson distribution). If $b > 1$, variance increases faster than the mean, indicating aggregation or clustering. And $b < 1$ means the uniform distribution.

Taylor (1961) also suggested that b was the species-specific constant. The coefficient a was considered to be a parameter of less ecological interest, but it does have an effect on the sampling stop line as discussed later on.

2. TPL Parameter Estimation in GLM

Taylor (1961) used log-log regression to estimate a and b in Taylor's Power law as in :

$$\log(s_i^2) = \log(a) + b\,\log(\bar{x}_i) + \epsilon_i, \quad i = 1,\, 2,\, \cdots,\, n \tag{3}$$

where $\hat{a}$, $\hat{b}$ are obtained by least squares estimation.

However, the population density could depends on the sampling date, region, or the phenological stage, and it is noted that measurement errors exist in the regression estimation Eq.(3) (Perry 1981).

Park and Cho (2004) used the quasi-likelihood with covariates, $\boldsymbol{x}_i$, such as in the mean model:

$$\log(\mu_i) = \boldsymbol{x}_i^T\boldsymbol{\beta}, \quad i = 1,\, 2,\, \cdots,\, n \tag{4}$$

and the variance model:

$$V(\mu_i) = a\,(\mu_i)^b = a\left(\exp\left(\boldsymbol{x}_i^T\boldsymbol{\beta}\right)\right)^b. \tag{5}$$

Given a and b, $\boldsymbol{\beta}$ is estimated by solving the estimating equation:

$$\boldsymbol{U(\beta) = D^T V^{-1}(Y - \mu) = 0,} \tag{6}$$

where D is an $n \times p$ derivative matrix of $\boldsymbol{\mu}$ defined as $D_{ij} = \partial\mu_i/\partial\beta_j$, V is the $n \times n$ variance matrix, $\mathbf{V}= diag\{Var(\mu_1), \cdots, Var(\mu_n)\}$, with $Var(\mu_i) = a\mu_i^b$ and $\mu_i = \exp(\boldsymbol{x_i^T\beta})$.

As for the estimation of a and b, the quasi-likelihood and variance function (QVF) modeling approach can be used, which maximizing the pseudo-likelihood given $\hat{\boldsymbol{\beta}}_*$:

$$l(\hat{\boldsymbol{\beta}}_*, a, b) = -\frac{n}{2}\log(a) - \frac{b}{2}\sum_{i=1}^{n} \boldsymbol{x}_i^T\hat{\boldsymbol{\beta}}_* - \sum_{i=1}^{n} \frac{\left(y_i - \exp\left(\boldsymbol{x}_i^T\hat{\boldsymbol{\beta}}_*\right)\right)^2}{2a\left(\exp\left(\boldsymbol{x}_i^T\hat{\boldsymbol{\beta}}_*\right)\right)^b} \tag{7}$$

as in (Carroll and Ruppert 1988, Carroll, Ruppert and Stefanski 1995) or, equivalently,

$$l(\hat{\boldsymbol{\beta}}_*, \boldsymbol{\lambda}) = -\frac{1}{2}\sum_{i=1}^{n} \boldsymbol{z_i^T\lambda} - \frac{1}{2}\sum_{i=1}^{n} \frac{\left(y_i - \exp\left(\boldsymbol{x_i^T}\hat{\beta}_*\right)\right)^2}{\exp(\boldsymbol{z_i^T\lambda})} \tag{8}$$

where $\boldsymbol{z_i}$=(1 $\boldsymbol{x_i^T}\hat{\boldsymbol{\beta}}_*$)^T and $\boldsymbol{\lambda}$=(log a b)^T. The $\hat{\boldsymbol{\lambda}}$ that maximizes Eq.(8) is the solution to the following quadratic estimating equation:

$$\frac{\partial l(\hat{\boldsymbol{\beta}}_*, \boldsymbol{\lambda})}{\partial \boldsymbol{\lambda}} = \frac{1}{2}\sum_{i=1}^{n}\left(\frac{(y_i - \exp(\boldsymbol{x_i^T}\hat{\boldsymbol{\beta}}_*))^2}{\exp(\boldsymbol{z_i^T\lambda})} - 1\right)\boldsymbol{z_i} = \mathbf{0}. \tag{9}$$

The above estimating equation coincides with that of the maximum likelihood estimator in the Gamma regression of the squared residual, $r_i^2 = (y_i - \exp(\boldsymbol{x_i^T}\hat{\boldsymbol{\beta}}_*))^2$, with a log link and scale parameter equal to 0.5, where

$$\begin{aligned} E(r_i^2) &= \exp(\boldsymbol{z_i^T\lambda}) \\ V(r_i^2) &= \frac{1}{2}\left(\exp(\boldsymbol{z_i^T\lambda})\right)^2. \end{aligned} \tag{10}$$

Park and Cho (2004) implemented GENMOD procedure (SAS Institute 2025) with a log link with the scaled deviance

$$D^*(y;\mu) = 2\int_{\mu}^{y} \frac{y-t}{at^b}dt. \tag{11}$$

in the mean model estimation, and they used another GENMOD procedure with a log link and a scale equal to .5 for gamma regression. They used the scaled deviance for mean model as the goodness of fit criterion (Breslow 1990).

3. Generalized Linear Mixed Model

It is well established that, in generalized linear models (GLM), the inclusion of random effects for some regression coefficients induces correlation among observations within the same group/cluster. This is called as Generalized Linear Mixed Model (GLMM) (Wolfinger and O'connell, 1993). In other words, if the regression coefficients $\boldsymbol{u}$ of covariates $\boldsymbol{z}$ follows $N(\boldsymbol{0}, G)$, the mean of y can be described as

$$g(\mu) = \boldsymbol{x}^T\boldsymbol{\beta} + \boldsymbol{z}^T\boldsymbol{u}, \quad \boldsymbol{u} \sim N(\boldsymbol{0}, G), \tag{12}$$

where $g(\cdot)$ is a link function.

When y_{ij} denotes the jth observation of the ith group(or cluster/panel), if the conditional probability density function $f(y_{ij}|\boldsymbol{u})$ belongs to the exponential family and $\boldsymbol{u}$ follows the multivariate normal distribution, and the link function is log, we could write it as

$$\mu_{ij}|\boldsymbol{u} = \exp\left(\boldsymbol{x}_{ij}^T\boldsymbol{\beta} + \boldsymbol{z}^T\boldsymbol{u}\right), \quad \boldsymbol{u} \sim N(\boldsymbol{0}, G). \tag{13}$$

Therefore, the joint likelihood function can be written as

$$L(\boldsymbol{\beta}) = \Pi_{i=1}^{a}\Pi_{j=1}^{n_i} \int f(y_{ij}|\boldsymbol{u}) f(\boldsymbol{u}) d\boldsymbol{u}. \tag{14}$$

And, there have been so many studies about maximizing the above quantity (Breslow and Clayton 1993, Wolfinger and O'connell 1993, Lee and Nelder 1996). The method approximates the GLMM by iteratively fitting a linear mixed model (LMM) to a working dependent (pseudo response) variable, derived from Taylor expansions. The steps are:

(Step1) Given the initial estimates: $\boldsymbol{\beta}^{(0)}$, $\boldsymbol{u}^{(0)}$, $\hat{a}^{(0)}$, $\hat{b}^{(0)}$

(Step2) Consider the working dependent variable $\boldsymbol{y}^{*(k)}$ as the linearization of $g(\boldsymbol{y})$ at the kth stage:

$$\boldsymbol{y}^{*(k)} = g(\boldsymbol{\mu}^{(k)}) + \left(\boldsymbol{y} - \boldsymbol{\mu}^{(k)}\right)\left(\frac{\partial \boldsymbol{\eta}}{\partial \boldsymbol{\mu}}\right) \tag{15}$$

where $\boldsymbol{\eta} = g(\boldsymbol{\mu}) = X\boldsymbol{\beta} + Z\boldsymbol{u}$ and the weight matrix

$$W^{(k)} = \text{diag}\left\{\text{Var}(y_i)^{-1}\left(\frac{d\mu_i}{d\eta_i}\right)^2\right\} \tag{16}$$

(Step3) Get the estimate $\boldsymbol{\beta}^{(k+1)}$ and $\boldsymbol{u}^{(k+1)}$ from the linear mixed model:

$$\boldsymbol{y}^{*(k)} = \underbrace{X\boldsymbol{\beta}^{(k+1)} + Z\boldsymbol{u}^{(k+1)}}_{\boldsymbol{\eta}^{(k+1)}} + \boldsymbol{e} \tag{17}$$

and

$$\begin{pmatrix} \boldsymbol{u} \\ \boldsymbol{e} \end{pmatrix} \sim N\left(\begin{pmatrix} \boldsymbol{0} \\ \boldsymbol{0} \end{pmatrix}, \begin{pmatrix} G(\boldsymbol{\theta}^{(k+1)}) & 0 \\ 0 & R(\boldsymbol{\theta}^{(k+1)}) \end{pmatrix} \right) \tag{18}$$

(Step4) The variance component estimates $\boldsymbol{\theta}^{(k+1)}$ is obtained via maximizing Restricted Pseudo-likelihood (REPL):

(19)
$$l_{REPL} = -\frac{1}{2}\log|V| - \frac{1}{2}\log|X^T V^{-1} X| - \frac{1}{2}(\boldsymbol{r}^T V^{-1}\boldsymbol{r}) - \frac{n-p}{2}\log(2\pi)$$

where n is the number of observation, p is the rank of X, $V = ZG(\boldsymbol{\theta}^{(k+1)})Z^T + R(\boldsymbol{\theta}^{(k+1)})$, and $\boldsymbol{r} = \boldsymbol{y}^{*(k)} - \boldsymbol{\eta}^{(k+1)}$.

(Step5) Iterate (Step2)-(Step4) until $\boldsymbol{\beta}$, $\boldsymbol{u}$, and $\boldsymbol{\theta}$ converge.

4. TPL Parameter Estimation in GLMM

In the light of Taylor's Power Law, we assume the followings in GLMM:

$$\begin{aligned} \mathrm{E}(y_i|\boldsymbol{\beta},\boldsymbol{u}) &= g^{-1}(\boldsymbol{x}_i^T\boldsymbol{\beta} + \boldsymbol{z}_i^T\boldsymbol{u}) \\ \mathrm{V}(y_i|\boldsymbol{\beta},\boldsymbol{u}) &= a\left\{g^{-1}(\boldsymbol{x}_i^T\boldsymbol{\beta} + \boldsymbol{z}_i^T\boldsymbol{u})\right\}^b \end{aligned} \tag{20}$$

Then, if $e_i = y_i - \mu_i = y_i - g^{-1}(\boldsymbol{x}_i^T\boldsymbol{\beta} + \boldsymbol{z}_i^T\boldsymbol{u})$, we consider

$$\begin{aligned} \mathrm{E}(\boldsymbol{e}|\boldsymbol{\beta},\boldsymbol{u}) &= \boldsymbol{0} \\ \mathrm{V}(\boldsymbol{e}|\boldsymbol{\beta},\boldsymbol{u}) &= R_{\boldsymbol{\mu}}^{1/2} R\, R_{\boldsymbol{\mu}}^{1/2} \end{aligned} \tag{21}$$

where R is the correlation matrix of $\boldsymbol{e}$ and $R_{\boldsymbol{\mu}}$ is the diagonal matrix with the entry

$$\{R_{\boldsymbol{\mu}}\}_{(i,i)} = a\left\{g^{-1}(\boldsymbol{x}_i^T\boldsymbol{\beta} + \boldsymbol{z}_i^T\boldsymbol{u})\right\}^b \tag{22}$$

The whole estimation process can be done within PROC GLIMMIX (SAS 2025) with a user-defined variance function based on Taylor's Power Law.

5. Sequential Sampling

Pest Management depends mainly on the right time and amount for the pesticides. In order to estimate the population density of a pest, it is essential to have a right stopping line for the sequential sampling scheme. Green (1970) presented stop lines for sequential sampling based on the Taylor's Power Law parameters, a and b. The sequential sampling stop line is defined as

$$\log T_n = \frac{\log(d_0^2/a)}{b-2} + \frac{b-1}{b-2}\log n, \tag{23}$$

where T_n is the cumulative number of pests in a sample of size n, d_0 is the fixed precision level defined as the ratio of the standard error to the mean, and a and b are the coefficients of Taylor's power law. Therefore, as the sequential sampling proceeds (n increases), T_n increases. If $\log(T_n)$ exceeds the stop line in Eq.(23), the sampling stops, and T_n/n will be the estimate for the mean pest density. This fixed-precision stop line has been widely used in agricultural and zoological sciences.

6. Concluding Remarks

Taylor's Power Law (TPL) represents an empirical relationship between the mean and variance of event counts, occurring across a wide range of domains including animal populations, social/natural phenomena, public health, and environmental sciences. Until now, the only covariate-based approach for estimating TPL coefficients was proposed by Park and Cho (2004). However, their method had a critical limitation: it could not be applied to correlated data structures (e.g., panel data, spatial data). This study methodologically proposes a novel approach for estimating Taylor's Power Law coefficients using correlated data. Furthermore, it demonstrates that this can be practically implemented through modification of the user-defined variance function in PROC GLIMMIX.

References

[1] L.R. Taylor (1961) *Aggregation, variance and the mean*, Nature 189:732–735.
[2] Meng Xu (2015) *Taylor's power law: before and after 50 years of scientific scrutiny*, ArXiv Prepr. (https://arxiv.org/pdf/1505.02033).
[3] J.E. Cohen (2016) *Statistics in primes (and probably twin primes) satisfy Taylor's law in ecology*, The American Statistician, Vol. 70 No. 4, 399–404.

[4] P. Shi, M. Li, Y. Li, J. Liu, H. Shi, S. Xie, and C. Yue (2019) *Taylor's power law in the Wenchuan earthquake sequence with fluctuation scaling*, Natural Hazards and Earth Science System Sciences, Vol.19, No.6. 1119–1127.
[5] J.E. Cohen and Meng Xu (2015) *Random sampling of skewed distributions implies Taylor's power law of fluctuation scaling*, Proc Natl Acad Sci USA Vol. 112, No.25, 7749–7754.
[6] J.N. Perry (1981) *Taylor's Power Law for dependence of variance on mean in animal population*, Applied Statistics, Vol. 30, 254–263.
[7] Heungsun Park and Kijong Cho (2004) *Use of covariates in Taylor's Power Law for sequential sampling in pest management*, Journal of Agricultural, Biological, and Environmental Statistics, Vol. 9, No. 4, 1–17.
[8] SAS Institute (2025) *The GLIMMIX Procedure* in SAS/STAT®15.3 User's Guide. Cary, NC: SAS Institute Inc.
[9] R.J. Carroll and D. Ruppert (1988) *Transformation and Weighting in Regression*, Chapman & Hall, London.
[10] R.J. Carroll, D. Ruppert, and L.A. Stefanski (1995) *Measurement Error in Nonlinear Models*, Chapman & Hall, London, 270.
[11] N. Breslow (1990) *Further studies in the variability of pock counts*, Statistics in Medicine, Vol. 9, 615–626.
[12] N.E. Breslow and D.G. Clayton (1993) *Approximate inference in generalized linear mixed models*, Journal of the American Statistical Association, Vol. 88, 9–25.

7. Author Information

Heungsun Park (hspark@hufs.ac.kr)
Professor, Department of Statistics, Hankuk University of Foreign Studies, South Korea.

J. Basic Sci. HUFS **60** (2025), pp. 8-14

AN EXPLICIT FORMULATION OF THE LEARNED NOISE PREDICTOR $\epsilon_\theta(\mathbf{x}_t, t)$ VIA THE FORWARD-PROCESS NOISE ϵ_t IN DENOISING DIFFUSION PROBABILISTIC MODELS (DDPMS)

KIHYUN YUN*

Abstract. In denoising diffusion probabilistic models (DDPMs), the learned noise predictor $\epsilon_\theta(\mathbf{x}_t, t)$ is trained to approximate the forward-process noise ϵ_t. The equality $\nabla_{\mathbf{x}_t} \log q(\mathbf{x}_t) = -\frac{1}{\sqrt{1-\bar{\alpha}_t}}\epsilon_\theta(\mathbf{x}_t, t)$ plays a fundamental role in both theoretical analyses and algorithmic design, and thus is frequently employed across diffusion-based generative models. In this paper, an explicit formulation of $\epsilon_\theta(\mathbf{x}_t, t)$ in terms of the forward-process noise ϵ_t is derived. This result shows how the forward-process noise ϵ_t contributes to the learned predictor $\epsilon_\theta(\mathbf{x}_t, t)$. Furthermore, based on this formulation, we present a novel and mathematically rigorous proof of the fundamental equality above, clarifying its origin and providing new theoretical insight into the structure of diffusion models.

1. Introduction

Denoising diffusion probabilistic models (DDPMs) is a basic framework for generative modeling, wherein a neural network $\epsilon_\theta(\mathbf{x}_t, t)$ is trained to predict the noise ϵ_t added in a forward diffusion process. In this paper, we use the definitions and notations as presented in DDPM paper [3]. A fundamental identity that appears repeatedly in diffusion-based generative models is

$$\nabla_{\mathbf{x}_t} \log q(\mathbf{x}_t) = -\frac{1}{\sqrt{1-\bar{\alpha}_t}}\epsilon_\theta(\mathbf{x}_t, t) \tag{1.1}$$

which connects the score function of the marginal distribution $q(\mathbf{x}_t)$ to the learned noise predictor $\epsilon_\theta(\mathbf{x}_t, t)$. Refer to [2, 4, 5]. This identity can be derived via Tweedie's formula, or alternatively as a byproduct of the reverse-time SDE framework established by Anderson [1]. Also refer to

* Department of Mathematics, Hankuk University of Foreign Studies, Yongin-si, Gyeonggi-do, South Korea. kihyun.yun@gmail.com.

[6]. However, both derivations do not clearly show how the forward-process noise ϵ_t contributes to the learned predictor $\epsilon_\theta(\mathbf{x}_t, t)$, and why it ends up matching the score function of the marginal distribution $q(\mathbf{x}_t)$ precisely.

In this work, we investigate this connection and provide an explicit formulation that expresses $\epsilon_\theta(\mathbf{x}_t, t)$ as the conditional expectation of the forward-process noise ϵ_t under the posterior $q(\mathbf{x}_0|\mathbf{x}_t)$. This perspective not only yields a novel and mathematically rigorous proof of the identity above, but also offers a clearer understanding of how the denoising objective implicitly captures the score of the marginal distribution. Our result describes the mathematical structure underlying DDPMs and reinforces the interpretation of noise prediction as a form of conditional averaging.

We begin by clarifying the definition of $\epsilon_\theta(\mathbf{x}_t, t)$. We use the definitions and notations as presented in DDPM paper [3], and thus refer to the paper [3] for details. Let $\mathbf{x}_0$ be a sample from the data distribution $q(\mathbf{x}_0)$. The forward diffusion process generates a sequence of latent variables $\mathbf{x}_1, \cdots, \mathbf{x}_T$ by gradually adding Gaussian noise. For each timestep $t = 1, \cdots, T$, the variable $\mathbf{x}_t$ in defined by

$$\mathbf{x}_t = \sqrt{\bar{\alpha}_t}\mathbf{x}_0 + \sqrt{1-\bar{\alpha}_t}\epsilon_t, \text{ where } \epsilon_t \sim \mathcal{N}(\mathbf{0}, \mathbb{I}).$$

Here, $\bar{\alpha}_t \in (0, 1)$ is the cumulative product of the noise schedule. It is worthy to note that ϵ_t is given by $\mathbf{x}_0$ and $\mathbf{x}_t$. Thus, we define a formal notation $\epsilon_t(\mathbf{x}_t|\mathbf{x}_0)$ for ϵ_t above as

$$\epsilon_t(\mathbf{x}_t|\mathbf{x}_0) = \epsilon_t.$$

From the definition of $\epsilon_\theta(\cdot, t)$ in DDPM, we find the parameter $\tilde{\theta}$ minimizing the expection

$$\mathbb{E}_{\mathbf{x}_0\sim q(\mathbf{x}_0)}\left[\mathbb{E}_{\epsilon_t\sim\mathcal{N}(\mathbf{0},\mathbb{I})}\left[\left\|\epsilon_t - \epsilon_{\tilde{\theta}}\left(\sqrt{\bar{\alpha}_t}\mathbf{x}_0 + \sqrt{1-\bar{\alpha}_t}\epsilon_t, t\right)\right\|^2\right]\right].$$

We define the function $\epsilon_\theta(\cdot, t)$ of $\mathbf{x}_t$ as

$$\begin{aligned}\epsilon_\theta(\cdot, t) &= f_*(\cdot) \\ &= \text{argmin}_{f(\cdot)}\mathbb{E}_{\mathbf{x}_0\sim q(\mathbf{x}_0)}\left[\mathbb{E}_{\epsilon_t\sim\mathcal{N}(\mathbf{0},\mathbb{I})}\left[\left\|\epsilon_t - f\left(\sqrt{\bar{\alpha}_t}\mathbf{x}_0 + \sqrt{1-\bar{\alpha}_t}\epsilon_t\right)\right\|^2\right]\right].\end{aligned}$$

Please note that the above f_* is not used commonly regardless of the choice of t. There is a different function f_* for each t.

THEOREM 1.1. *Let $\epsilon_\theta(\cdot, t)$ and $\epsilon_t(\mathbf{x}_t|\mathbf{x}_0)$ be as given above. Then, we have*

$$\epsilon_\theta(\mathbf{x}_t, t) = \int_{\Omega(\mathbf{X}_0)} \epsilon_t(\mathbf{x}_t|\mathbf{x}_0) q(\mathbf{x}_0|\mathbf{x}_t) d\mathbf{x}_0.$$

where $\Omega(\mathbf{X}_0)$ is the domain of $\mathbf{X}_0$.

The proof is presented in Section 2. The representation of $\epsilon_\theta(\mathbf{x}_t, t)$ is reasonable by noting that, since $\epsilon_\theta(\mathbf{x}_t, t)$ is a function of $\mathbf{x}_t$, it should be considered under the condition with $\mathbf{x}_t$ is given, and consequently, the distribution of $q(\mathbf{x}_0|\mathbf{x}_t)$ is used to describe $\epsilon_\theta(\mathbf{x}_t, t)$.

The preceding theorem provides a natural derivation of the fundamental identity (1.1), which is also stated in the following corollary.

COROLLARY 1.1.

$$\nabla_{\mathbf{x}_t} \log q(\mathbf{x}_t) = -\frac{1}{\sqrt{1-\bar{\alpha}_t}} \epsilon_\theta(\mathbf{x}_t, t).$$

The equality is found in (11) in [2]. The following provides a new derivation the equality above derived from Theorem 1.1.

Proof of Corollary 1.1. We begin by considering

$$\epsilon_t(\mathbf{x}_t|\mathbf{x}_0) = \epsilon_t, \quad \text{and } \mathbf{x}_t = \sqrt{\bar{\alpha}_t}\mathbf{x}_0 + \sqrt{1-\bar{\alpha}_t}\epsilon_t,$$

where $\epsilon_t \sim \mathcal{N}(\mathbf{0}, \mathbb{I})$. Then we have

$$\frac{\mathbf{x}_0 - \sqrt{\bar{\alpha}_t}\mathbf{x}_0}{\sqrt{1-\bar{\alpha}_t}} = \epsilon_t(\mathbf{x}_t|\mathbf{x}_0) \sim \mathcal{N}(\mathbf{0}, \mathbb{I}), \tag{1.2}$$

$$q(\mathbf{x}_t|\mathbf{x}_0) = p(\epsilon_t(\mathbf{x}_t|\mathbf{x}_0)|\mathbf{x}_0) = \mathcal{N}(\epsilon_t(\mathbf{x}_t|\mathbf{x}_0)|\mathbf{0}, \mathbb{I}). \tag{1.3}$$

In details,

$$q(\mathbf{x}_t|\mathbf{x}_0) = \mathcal{N}(\mathbf{x}_t|\sqrt{\bar{\alpha}_t}\mathbf{x}_0, (1-\bar{\alpha}_t)\mathbb{I}) = \frac{1}{Z}\exp\left(-\frac{1}{2(1-\bar{\alpha}_t)}\left\|\mathbf{x}_t - \sqrt{\bar{\alpha}_t}\mathbf{x}_0\right\|^2\right).$$

Then, by the relation (1.2),

$$\begin{aligned}\nabla_{\mathbf{x}_t} \log q(\mathbf{x}_t|\mathbf{x}_0) &= -\frac{1}{1-\bar{\alpha}_t}\left(\mathbf{x}_t - \sqrt{\bar{\alpha}_t}\mathbf{x}_0\right) \\ &= -\frac{1}{\sqrt{1-\bar{\alpha}_t}}\epsilon_t(\mathbf{x}_t|\mathbf{x}_0). \end{aligned} \tag{1.4}$$

Applying (1.4) to the result of Theorem 1.1,

$$\begin{aligned}
\epsilon_\theta(\mathbf{x}_t, t)q(\mathbf{x}_t) &= \left(\int_{\Omega(\mathbf{x}_0)} \epsilon_t(\mathbf{x}_t|\mathbf{x}_0)q(\mathbf{x}_0|\mathbf{x}_t)d\mathbf{x}_0\right) q(\mathbf{x}_t) \\
&= \int_{\Omega(\mathbf{x}_0)} \epsilon_t(\mathbf{x}_t|\mathbf{x}_0)q(\mathbf{x}_t, \mathbf{x}_0)d\mathbf{x}_0 \\
&= \int_{\Omega(\mathbf{x}_0)} -\sqrt{1-\bar{\alpha}_t}\Big(\nabla_{\mathbf{x}_t} \log q(\mathbf{x}_t|\mathbf{x}_0)\Big)q(\mathbf{x}_t|\mathbf{x}_0)q(\mathbf{x}_0)d\mathbf{x}_0 \\
&= -\sqrt{1-\bar{\alpha}_t} \int_{\Omega(\mathbf{x}_0)} \left(\frac{\nabla_{\mathbf{x}_t} q(\mathbf{x}_t|\mathbf{x}_0)}{q(\mathbf{x}_t|\mathbf{x}_0)}\right) q(\mathbf{x}_t|\mathbf{x}_0)q(\mathbf{x}_0)d\mathbf{x}_0 \\
&= -\sqrt{1-\bar{\alpha}_t}\nabla_{\mathbf{x}_t} \int_{\Omega(\mathbf{x}_0)} \left(\frac{q(\mathbf{x}_t, \mathbf{x}_0)}{q(\mathbf{x}_0)}\right) q(\mathbf{x}_0)d\mathbf{x}_0 \\
&= -\sqrt{1-\bar{\alpha}_t}\nabla_{\mathbf{x}_t} \int_{\Omega(\mathbf{x}_0)} q(\mathbf{x}_t, \mathbf{x}_0)d\mathbf{x}_0 \\
&= -\sqrt{1-\bar{\alpha}_t}\nabla_{\mathbf{x}_t} q(\mathbf{x}_t).
\end{aligned}$$

Then,

$$\epsilon_\theta(\mathbf{x}_t, t) = -\sqrt{1-\bar{\alpha}_t}\frac{\nabla_{\mathbf{x}_t} q(\mathbf{x}_t)}{q(\mathbf{x}_t)} = -\sqrt{1-\bar{\alpha}_t}\nabla_{\mathbf{x}_t} \log q(\mathbf{x}_t).$$

Thus, we have this corollary. □

2. Proof of the theorem 1.1

Although a fully rigorous proof would require explicitly specifying the appropriate function space and proceeding accordingly, we have chosen instead to present a concise proof that reveals the core idea behind the argument. This approach is intended to make the content more accessible to a broader readers, including readers without a background in mathematics.

From the definition of $\epsilon_t(\mathbf{x}_t|\mathbf{x}_0)$, the expectation to be minimized for defining the function $\epsilon_\theta(\mathbf{x}_t, t)$ can be reformulated and understood in the following form:

$$\begin{aligned}
&\mathbb{E}_{\mathbf{x}_0\sim q(\mathbf{x}_0)}\left[\mathbb{E}_{\epsilon_t=\epsilon_t(\mathbf{x}_t|\mathbf{x}_0)\sim\mathcal{N}(\mathbf{0},\mathbb{I})}\left[\left\|\epsilon_t - \epsilon_\theta\left(\sqrt{\bar{\alpha}_t}\mathbf{x}_0 + \sqrt{1-\bar{\alpha}_t}\epsilon_t, t\right)\right\|^2\right]\right] \\
&= \mathbb{E}_{\mathbf{x}_0\sim q(\mathbf{x}_0)}\left[\mathbb{E}_{\epsilon_t\sim\mathcal{N}(\mathbf{0},\mathbb{I})}\left[\left\|\epsilon_t - \epsilon_\theta\left(\mathbf{x}_t, t\right)\right\|^2 \;\middle|\; \mathbf{x}_t = \sqrt{\bar{\alpha}_t}\mathbf{x}_0 + \sqrt{1-\bar{\alpha}_t}\epsilon_t\right]\right],
\end{aligned}$$

and the function $\epsilon_\theta(\cdot, t)$ of $\mathbf{x}_t$ is a function $f_*(\cdot)$ minimizing the expectation as follows:

(2.1)
$$\begin{aligned}
&\epsilon_\theta(\cdot, t) = f_*(\cdot) \\
&= \text{argmin}_{f(\cdot)} \\
&\mathbb{E}_{\mathbf{x}_0 \sim q(\mathbf{x}_0)} \left[\mathbb{E}_{\epsilon_t(\mathbf{x}_t|\mathbf{x}_0) \sim \mathcal{N}(\mathbf{0}, \mathbb{I})} \left[\left\| \epsilon_t(\mathbf{x}_t|\mathbf{x}_0) - f(\mathbf{x}_t) \right\|^2 \;\middle|\; \mathbf{x}_t = \sqrt{\bar{\alpha}_t}\mathbf{x}_0 + \sqrt{1-\bar{\alpha}_t}\epsilon_t(\mathbf{x}_t|\mathbf{x}_0) \right] \right] \\
&= \text{argmin}_{f(\cdot)} \mathbb{E}_{\mathbf{x}_0 \sim q(\mathbf{x}_0)} \left[\mathbb{E}_{\mathbf{x}_t \sim q(\mathbf{x}_t|\mathbf{x}_0)} \left[\left\| \epsilon_t(\mathbf{x}_t|\mathbf{x}_0) - f(\mathbf{x}_t) \right\|^2 \right] \right].
\end{aligned}$$

Let $h(\cdot)$ be arbitrary function, and s be a real number. Then,

$$(f_* + sh)(\mathbf{x}_t) = f_*(\mathbf{x}_t) + sh(\mathbf{x}_t).$$

At $s = 0$, the function $(f_* + sh)(\mathbf{x}_t)$ minimizes the following expection

$$F_h(s) = \mathbb{E}_{\mathbf{x}_0 \sim q(\mathbf{x}_0)} \left[\mathbb{E}_{\mathbf{x}_t \sim q(\mathbf{x}_t|\mathbf{x}_0)} \left[\left\| \epsilon_t(\mathbf{x}_t|\mathbf{x}_0) - (f_* + sh)(\mathbf{x}_t) \right\|^2 \right] \right].$$

Let $\Omega(\mathbf{x}_t)$ be the set of all $\mathbf{x}_t$, and it is the common domain of f_* and h. Then,

$$\begin{aligned}
0 &= \frac{dF_h}{ds}(0) \\
&= \mathbb{E}_{\mathbf{x}_0 \sim q(\mathbf{x}_0)} \left[\mathbb{E}_{\mathbf{x}_t \sim q(\mathbf{x}_t|\mathbf{x}_0)} \left[2\left(\epsilon_t(\mathbf{x}_t|\mathbf{x}_0) - f_*(\mathbf{x}_t)\right) h(\mathbf{x}_t) \right] \right] \\
&= 2 \int_{\Omega(\mathbf{x}_0)} \left(\int_{\Omega_{(\mathbf{x}_t)}} \left(\epsilon_t(\mathbf{x}_t|\mathbf{x}_0) - f_*(\mathbf{x}_t)\right) h(\mathbf{x}_t) q(\mathbf{x}_t|\mathbf{x}_0) d\mathbf{x}_t \right) q(\mathbf{x}_0) d\mathbf{x}_0 \\
&= 2 \int_{\Omega(\mathbf{x}_t)} \left(\int_{\Omega_{(\mathbf{x}_0)}} \left(\epsilon_t(\mathbf{x}_t|\mathbf{x}_0) - f_*(\mathbf{x}_t)\right) q(\mathbf{x}_t|\mathbf{x}_0) q(\mathbf{x}_0) d\mathbf{x}_0 \right) h(\mathbf{x}_t) d\mathbf{x}_t
\end{aligned}$$

(2.2)
$$= 2 \int_{\Omega(\mathbf{x}_t)} g(\mathbf{x}_t) h(\mathbf{x}_t) d\mathbf{x}_t,$$

where

$$g(\mathbf{x}_t) = \int_{\Omega(\mathbf{x}_0)} \left(\epsilon_t(\mathbf{x}_t|\mathbf{x}_0) - f_*(\mathbf{x}_t)\right) q(\mathbf{x}_t|\mathbf{x}_0) q(\mathbf{x}_0) d\mathbf{x}_0.$$

Note that g is regardless of h. Since h is an arbitrary function, the equality (2.2) implies

$$\begin{aligned}
0 = g(\mathbf{x}_t) &= \int_{\Omega(\mathbf{x}_0)} \left(\epsilon_t(\mathbf{x}_t|\mathbf{x}_0) - f_*\left(\mathbf{x}_t\right)\right) q(\mathbf{x}_t|\mathbf{x}_0) q(\mathbf{x}_0) d\mathbf{x}_0 \\
&= \int_{\Omega(\mathbf{x}_0)} \left(\epsilon_t(\mathbf{x}_t|\mathbf{x}_0) - f_*\left(\mathbf{x}_t\right)\right) q(\mathbf{x}_t, \mathbf{x}_0) d\mathbf{x}_0 \\
&= \int_{\Omega(\mathbf{x}_0)} \epsilon_t(\mathbf{x}_t|\mathbf{x}_0) q(\mathbf{x}_t, \mathbf{x}_0) d\mathbf{x}_0 - f_*\left(\mathbf{x}_t\right) \int_{\Omega_{(\mathbf{x}_0)}} q(\mathbf{x}_t, \mathbf{x}_0) d\mathbf{x}_0 \\
&= \int_{\Omega(\mathbf{x}_0)} \epsilon_t(\mathbf{x}_t|\mathbf{x}_0) q(\mathbf{x}_t, \mathbf{x}_0) d\mathbf{x}_0 - f_*\left(\mathbf{x}_t\right) q(\mathbf{x}_t).
\end{aligned}$$

Then,

$$\begin{aligned}
\epsilon_\theta(\mathbf{x}_t, t) &= f_*\left(\mathbf{x}_t\right) \\
&= \frac{1}{q(\mathbf{x}_t)} \int_{\Omega(\mathbf{x}_0)} \epsilon_t(\mathbf{x}_t|\mathbf{x}_0) q(\mathbf{x}_t, \mathbf{x}_0) d\mathbf{x}_0 \\
&= \int_{\Omega(\mathbf{x}_0)} \epsilon_t(\mathbf{x}_t|\mathbf{x}_0) q(\mathbf{x}_0|\mathbf{x}_t) d\mathbf{x}_0
\end{aligned}$$

Thus, we have the desirable result. □

References

[1] B. D. O. Anderson, *Reverse-time diffusion equation models (1982)*, Stochastic Processes and their Applications, Volume 12, Issue 3,1982, pp. 313-326.

[2] Prafulla Dhariwal and Alex Nichol(2021), *Diffusion Models Beat GANs on Image Synthesis*, arXiv:2105.05233, NeuriPS 21, Article No. 672, pp. 8780 - 8794.

[3] Jonathan Ho, Ajay Jain, and Pieter Abbeel (2020) *Denoising diffusion probabilistic models*, arXiv:2006.11239, NeuriPS 20, Article No. 574, pp. 6840 - 685.

[4] Jonathan Ho and Tim Salimans (2021), *Classifier-Free Diffusion Guidance*, arXiv:2207.12598, NeurIPS 21 Workshop on Deep Generative Models and Downstream Applications.

[5] Alex Nichol, Prafulla Dhariwal, Aditya Ramesh, et al. (2022), *GLIDE: Towards Photorealistic Image Generation and Editing with Text-Guided Diffusion Models*, ICML.

[6] Yang Song, Jascha Sohl-Dickstein, Diederik P Kingma, Abhishek Kumar, Stefano Ermon and Ben Poole(2021), *Score-Based Generative Modeling through Stochastic Differential Equations*, ICLR.

3. Author Information

KiHyun Yun (kihyun.yun@gmail.com)

Professor, Department of Mathematics, Hankuk University of Foreign Studies, South Korea.

J. Basic Sci., HUFS, **60** (2025), pp. 15-19

Bacteriophage Therapy in Industry: A New Horizon in Antibacterial Treatment[1]

Heejoon Myung[2]

ABSTRACT: Bacteriophage therapy is re-emerging as a promising approach in the fight against antimicrobial-resistant (AMR) bacteria. This paper reviews the current industrial landscape of bacteriophage applications, including therapeutic strategies, clinical trials, and regulatory frameworks. With rising AMR and limited new antibiotics, phages provide a highly specific, safe, and effective alternative. This review emphasizes both clinical applications and future directions for industrial-scale phage-based therapeutics.

1. Introduction

Bacteriophages are viruses that infect bacteria, representing the most abundant biological entities on Earth. Each bacterium can be susceptible to infection by multiple phages, making them powerful natural antibacterial agents. With the global crisis of antimicrobial resistance (AMR) growing rapidly, new strategies beyond traditional antibiotics are urgently needed. Bacteriophage therapy has gained renewed attention, especially within industry-led developments aiming to provide scalable and effective treatments.

2. Medical applications and clinical trials

There are two major pathways for clinical bacteriophage therapy: personalized phage cocktails administered under emergency IND (eIND) protocols by hospitals, and fixed cocktail products developed through company-sponsored clinical trials. The former relies on phage libraries and patient-specific formulations, while the latter targets scalable solutions. Indications range from respiratory and skin infections to osteomyelitis and urinary tract infections (UTIs). There are numerous eIND-based phage therapy centers operating in the

[1] This research was supported by the research fund 2025 of Hankuk University of Foreign Studies.
[2] Department of Bioscience and Biotechnology, Hankuk University of Foreign Studies, Yongin 17035, Republic of Korea. E-mail: hjmyung@hufs.ac.kr

world, including Queen Astrid Military Hospital in Belgium, 16 clinical centers belonging to Phage Australia, IPATH in UCSD, Tailor in Baylor, Mayo Clinic, and Yale University. Phage Canada and Phage UK have also started. Traditional centers like Eliava in Georgia and Hirszfeld in Poland are also operating (Figure 1).

Figure 1. Phage therapy clinical centers around the world.

Usually, the centers admit patient with non-curable bacterial infections, identify the pathogen of interest, screen the phage library and select for best phage cocktail, produce phages for administration (non GMP), treat the patient with the phages, and monitor the outcome. These kinds of clinical treatments have shown promise. One study [1] reported 77.2% clinical improvement and 61.3% eradication rates, though phage resistance developed in 43.8% of patients. Phage-antibiotic synergy was observed in 90% of tested cases, highlighting combinatorial potential. Adverse effects were typically mild or non-serious. The other category of phage therapy uses fixed phage cocktail for off-the-shelf treatments. An example includes LBP-EC01, a CRISPR-Cas3-enhanced cocktail targeting *E. coli* in UTIs, demonstrating rapid bacterial clearance post-treatment with no serious adverse events [2].

3. Industrial and global development landscape

Phage therapy development has largely been led by private initiatives rather than government bodies. Collaborative hospital consortia such as Phage Australia and Belgian initiatives exemplify the eIND model, whereas companies like Locus Biosciences have entered late-stage trials for fixed phage products. The U.S. NIH is one of the few public institutions running government-sponsored phage trials, including a phase 1b/2a trial targeting P. aeruginosa in cystic fibrosis patients. In Korea, the Phage Korea Initiative started by government and academic stakeholders in 2024 and aimed to start its first clinical trial in 5 years.

4. Regulatory frameworks and challenges

Globally, regulatory frameworks for phage therapy vary widely. The U.S. FDA allows eIND-based compassionate use; Australia uses the Special Access Scheme (SAS); and the EU permits use under the Magistral Formula exception. The UK allows non-GMP phage imports for compassionate use. However, many countries, including Korea, lack appropriate frameworks, hindering wider clinical adoption. Major challenges also include variable pharmacokinetics, host immune responses, bacterial resistance evolution, and standardization of phage production [3].

5. Beyond whole phages: phage-derived enzymes

Phage-derived enzymes, particularly endolysins, are gaining interest as novel antimicrobial agents. These recombinant proteins demonstrate high specificity and can act against both Gram-positive and Gram-negative bacteria. Their use opens new industrial avenues beyond traditional phage therapy. One example is an engineered endolysin targeting Gram-negative pathogens. Contrary to Gram-positives, they have outer membrane barrier hindering endolysin’s access to cell wall. Very few natural endolysins showed intrinsic antibacterial activity and fusion of antimicrobial peptide is a way of enhancing the efficacy [4]. There are a few endolysins in clinical trial.

6. Veterinary and agricultural applications

In livestock, phage-based feed additives help prevent infections without contributing to antibiotic resistance. Since the ban on antibiotics in livestock industry, phages quickly gained attention as feed additives. Phage cocktails targeting *Salmonella gallinarum* is being marketed in Korea by Intron Bio and OptiPharm. Protheon in Poland is also developing the same phage products. In agriculture, phages are being explored for managing bacterial plant diseases, such as fire blight. The phage products are marketed by OmniLytics in the US and PhageLux in China. These applications highlight the versatility of phages beyond human medicine.

7. Conclusion

Bacteriophage therapy stands as a promising frontier in combating antibiotic resistance. Industrial involvement is crucial for transitioning from personalized therapies to mass-produced, regulated products. Continued research, policy development, and investment will determine the future impact of phages in global health.

References

[1] Pirnay JP et al. 2024. Personalized bacteriophage therapy outcomes for 100 consecutive cases: a multicentre, multinational, retrospective observational study. *Nature Microbiology* 9**:** 1434

[2] Kim P et al. 2024. Safety, pharmacokinetics, and pharmacodynamics of LBP-EC01, a CRISPR-Cas3-enhanced bacteriophage cocktail, in uncomplicated urinary tract infections due to Escherichia coli (ELIMINATE): the randomised, open-label, first part of a two-part phase 2 trial. *The Lancet Infectious Diseases* 24: 1319

[3] Zalewska-Pia˛tek, B. 2023. Phage Therapy—Challenges, Opportunities and Future Prospects. *Pharmaceuticals* 16: 1638

[4] Hong H-W et al. 2025. In vitro and in vivo efficacy studies of an engineered endolysin targeting Gram negative pathogens. *International Journal of Biological Macromolecules* 302:140463

저자정보

주저자 and 교신저자: Heejoon Myung / Department of Bioscience and Biotechnology / professor

J. Basic Sci., HUFS, **60** (2025), pp. 20-25

Screening of potential immunosuppressive compounds that inhibit transcriptional activity of the Nuclear Factor of Activated T cell [1]

Jungchan Park [2]

ABSTRACT: To find substances that inhibit the activity of the transcription factor NFAT, which plays an important role in inducing immune activation, ten compounds were selected from the compound library held by the Korea Research Institute of Chemical Technology (KRICT). Among the selected compounds, three showed high inhibitory activity. Compounds with similar skeletal structures to these three were obtained from a collaborating institution. Their NFAT activation inhibition and cytokine production inhibition were then measured in Jurkat cell line. The activity analysis of these hit compounds will be utilized for the development of lead compounds for novel immunosuppressants.

Introduction

While the immune response protects our bodies by eliminating invading pathogens, its excessive or skewed intensity can be harmful, necessitating the suppression of immune activity for therapeutic purposes. Nuclear factor of activated T cells (NFAT) is a transcription factor crucial for inducing and regulating immune responses in activated immune cells. It plays a vital role in the expression of various cytokine genes (e.g., IL-2, -3, -4, -5, GM-CSF, TNF-α, IFN-γ) and cell surface factors (e.g., CD40L, FasL, IL-2Rα) (1, 2). Studies have shown a correlation between NFAT functional defects and significantly deficient cytokine gene expression in some patients with severe immunodeficiency (2).

It is known that the highly effective immunosuppressive agents Cyclosporin A (CsA) and FK-506, widely used in clinical settings, interfere with cytokine production primarily by inhibiting NFAT function (3, 4). This suggests that by developing new methods to inhibit NFAT function directly, as a final effector transcription factor rather than an intermediate intracellular signaling mediator like calcineurin, we can potentially achieve novel

[1] This research was supported by the research fund 2025 of Hankuk University of Foreign Studies.
[2] Department of Bioscience and Biotechnology, Hankuk University of Foreign Studies, Yongin 17035, Republic of Korea. E-mail: jpark@hufs.ac.kr

immunosuppressive strategies with reduced side effects compared to existing immunosuppressants (2, 5).

Previously, we have developed a Jurkat NFAT cell line stably transfected with an NFAT reporter gene construct (6). In this study, to develop novel immunosuppressants targeting NFAT, we screened a compound library consisting of 4480 compounds using the Jurkat NFAT cell line. From this screening, we obtained several candidate compounds that effectively inhibited NFAT transcriptional activity and investigated their inhibitory effects on cytokine production.

Materials and methods

Cell Line and Culture

Jurkat and Jurkat NFAT cell lines were cultured in RPMI 1640 (GibcoBRL, USA) supplemented with 10% Fetal bovine serum (HyClone, USA), 2 mM L-glutamine, and 100 U penicillin/streptomycin. Cells were maintained in a 37 ℃, 5% CO_2 incubator. When necessary, cells were stimulated with 20 ng/ml PMA and 2 μM ionomycin. A 1 μM concentration of CsA was used as a positive control for NFAT activity inhibition.

NFAT Activity Assay

The analysis of NFAT activity inhibition by small chemical compounds was performed using the Jurkat NFAT cell line, which was created by stably integrating the NFAT reporter construct, pNFAT-gal, into the Jurkat cell genome (6). The assay employed a 24-well plate format, and final results were obtained from at least 2-3 repeated experiments. For each sample, 7 x 10^5 cells/well were seeded into a 24-well plate. Cells were then activated with 20 ng/ml PMA (Sigma, USA) and 2 μM ionomycin (Sigma, USA). After adding the sample compounds at predetermined concentrations, the cells were incubated for 6 hours at 37 ℃. Cells were harvested into 1.5 ml tubes, washed once with 500 μl of 1x PBS, and lysed by adding 110 μl of 1x reporter lysis buffer (Promega, USA). The lysates were then centrifuged

at 12,000 rpm for 10 minutes at 4 ℃, and the cell lysate was transferred to a new tube.

20-30 μl of cell extract was added to a 96-well dark plate along with 150 μl of β-galactosidase (NFAT activity) assay reaction solution and incubated for 30 minutes at 37 ℃. The composition of the reaction solution was as follows: 1 mM $MgCl_2$, 50 μM 2-Mercaptoethanol, 1 mM 4-methyl-umbellifery-galactoside (MUG), and 100 mM sodium phosphate buffer, pH 7.3. After the reaction, the fluorescence of the reaction product, 4-methyl-umbelliferone, was measured using a Fluoro/Lumino-combined plate reader (Fusion TR-FRET, Packard Bioscience) at excitation: 440nm and emission: 365nm.

Assay for cytokine production

For each sample, 1 x 10^5 cells/well were seeded into a 96-well plate. Cells were then activated with 20 ng/ml PMA (Sigma, USA) and 2 μM ionomycin (Sigma, USA). After adding the sample compounds at predetermined concentrations, the cells were incubated for 24 hours at 37 ℃. According to manufacturer's protocol, productions of several cytokines such as IL-2, GM-CSF, TNF-a, and IL-4 in each culture supernatant were measured using commercial human cytokine ELISA kits (R&D system, USA).

Results and Discussion

Screening a chemical library from KRICT

To identify compounds that inhibit the activity of the transcription factor NFAT, we were provided with a compound library held by the Korea Research Institute of Chemical Technology (KRICT). This library, comprising 4,480 organic compounds from various companies and institutions, was screened. We utilized a previously developed Jurkat NFAT cell line to measure NFAT transcriptional activity and assess general cytotoxicity via MTT assay (6). As a result, we successfully identified 10 compounds that inhibit NFAT transcriptional activity without exhibiting general cytotoxicity. The inhibitory activities of the selected compounds were from 95 % to 65% at 2.5 μM treatment. Their activities are presented in Figure 1.

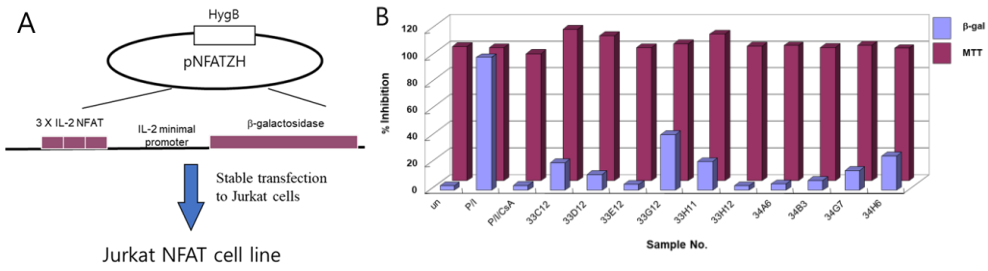

Fig 1. Inhibition of NFAT-dependent transcription by selected chemical compounds from KRICT**. (A)** Jurkat NFAT cell line containing an NFAT-dependent reporter gene stably integrated into the genome. (B) Inhibition of NFAT-dependent transcription by selected compounds. Using the Jurkat NFAT cell lines, a chemical library consisting of 4480 small organic chemicals was screened, and 10 potential candidates were selected.

Inhibitory analysis of NFAT Activity and Cytokine Production for Hanwha Compounds

Among the 10 hit compounds selected through the exploration of the KRICT library, 33H12, 34A6, and 34B3 were compounds submitted by Hanwha and showed relatively high NFAT inhibitory activity. Consequently, Hanwha provided an additional 8 structurally similar compounds, and their ability to inhibit NFAT transcriptional activity was measured at concentrations of 1 μM and 0.5 μM (Fig. 2A). As a result, six of these compounds, excluding 4213 I® and 4213 T®, showed over 70% inhibition even at 0.5 μM, and exhibited stronger inhibitory effects at 1 μM than at 0.5 μM.

To confirm whether these compounds inhibit cytokine production, we analyzed the inhibition of IL-2, IL-4, GM-CSF, and TNF-α cytokine production by these compounds in Jurkat T cells activated with PMA and ionomycin (Fig. 2B). Generally, all compounds showed inhibitory effects, but 4213 I® and 4213 T® showed relatively lower cytokine production inhibitory activity compared to other compounds, particularly very low inhibitory activity for TNF-α and IL-4. These results are consistent with the NFAT transcriptional activity inhibition results, implying that NFAT transcriptional activity plays a crucial role in the production of the four aforementioned cytokines.

To quantitatively compare the NFAT activity inhibition and IL-2 production inhibition

capabilities of these 8 compounds, their IC_{50} values were measured (Fig. 2C). The results generally showed a correlation between NFAT activity inhibition and IL-2 production inhibition. The compounds 4213 I® and 4213 T®, which previously showed relatively low NFAT activity inhibition and cytokine production inhibition, exhibited IC_{50} values greater than 500 nM for NFAT activity inhibition, and 2830 nM and 873 nM, respectively, for IL-2 production inhibition. Among the 8 compounds, 4213 I showed the strongest inhibitory activity with an IC_{50} value of 15 nM for NFAT activity inhibition and 174 nM for IL-2 production inhibition.

A

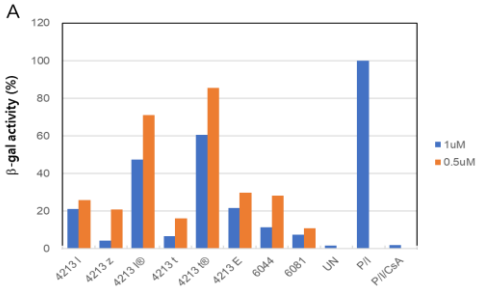

B

Compounds conc. (treated hours)	1uM (24hr)	1uM (24hr)	10uM (5hr)	10uM (23hr)
Cytokines	IL-2	GM-CSF	TNF-α	IL-4
4213 I	99	100	99	77
4213 T	95	109	93	47
4213 Z	100	102	100	77
4213 E	98	102	99	87
6044	100	105	94	83
6081	95	92	92	98
4213 I(R)	75	76	12	-17
4213 T(R)	71	69	68	55
CsA	100	97	96	113

C

Chemical code	4213 I	4213 I®	4213 Z	4213 T®	4213 T	4213 E	6081	6044	CsA
NFAT (nM)	15	520	22	650	74	61	40	52	2
IL-2 (nM)	174	2830	417	873	185	376	158	502	12

Fig. 2. Inhibition of NFAT transcriptional activity and cytokine production by selected Hanwha chemicals. (A) NFAT activity test by the selected Hanwha chemicals. Two different concentration of compounds (0.5 μM and 1 μM) were tested. NFAT-dependent β-galactosidase assay was done with Jurkat NFAT cells after stimulated with PMA and ionomycin. (B) Inhibition of cytokine production by the selected Hanwha chemicals. Jurkat cells were stimulated with PMA and ionomycin in the presence of Hanwha chemicals as indicated. IL-2, GM-CSF, TNF-α, and IL-4 production were measured as described in Material and Methods. (C) IC_{50} values of Hanwha chemicals for NFAT activity and IL-2 production. IC_{50} values were measured in Jurkat cells.

Acknowledgements

이 연구는 2025년 한국외국어대학교 학술연구비 지원에 의해 이루어진 것임.

References

[1] Rao, A., Luo, C., and Hogan, P.G. (1997) *Annu. Rev. Immunol*. 15; 707-747

[2] Kiani, A., Rao, A., and Aramburu, J. (2000*) Immunity* 12:359-372 22.

[3] Shaw, J.P., Utz, P.J., Durand, D.B., Toole, J.J., Emmel, E.A., and Crabtree, G.R. (1988) *Science* 241:202-205

[4] Shaw, K. T. -Y, Ho, A. M., Raghavan, A., Kim, J., Jain, J., Park, J., Sharma, S., Rao, A., and Hogan, P. G. (1995*) Proc. Natl. Acad. Sci*. USA 92, 11205-11209.

[5] Lee, M. and Park, J. (2006) *Mol. Cells* 22; 1-7

[6] Chun, Y. and Park, J. (2012) *J. Basic Sci*., HUFS 33:1-7.

저자정보

교신저자 : 박중찬 / 생명공학과 / 교수

J. Basic Sci., HUFS, **60** (2025), pp. 26-33

Decoupling Doping Magnitude and Uniformity in Photoexcited WSe_2/BN Heterostructures[1]

Taekyeong Kim[2]

ABSTRACT: Photoinduced doping in 2D material heterostructures offers a powerful means to modulate electronic properties without physical contacts. In WSe_2/BN heterostructures, the thickness of the BN layer and the duration of optical illumination critically influence the extent and uniformity of doping. While thicker BN enhances the overall doping level, the spatial uniformity remains largely unaffected by thickness. However, extended light exposure leads to a more homogeneous doping profile, driven by the redistribution of defect-induced charges within the BN layer.

Introduction

In WSe_2/BN heterostructures, the photoinduced doping effect (ΔV) increases with BN thickness, while the doping inhomogeneity, indicated by the full width at half maximum (FWHM), remains unaffected. This suggests that although thicker BN enhances the overall doping level, it does not impact the spatial uniformity of doping. To further investigate the dynamic behavior of doping inhomogeneity, time-dependent ΔV mapping was conducted on a 94 nm BN sample. The results show that longer illumination times lead to reduced spatial variation in ΔV, implying improved doping uniformity. This effect is attributed to the gradual redistribution of defect charges within the BN layer, which enhances electric field screening and reduces nanoscale charge disorder.

Experimental

[1] This research was supported by the research fund 2025 of Hankuk University of Foreign Studies.
[2] Department of Physics, Hankuk University of Foreign Studies, Yongin 17035, Republic of Korea. E-mail: tkim@hufs.ac.kr

To further examine the thickness-dependent variation in the photoinduced doping of BN, ΔV imaging was performed on WSe_2/BN heterostructures with varying BN thicknesses. Figures 4(a), (b), (c), and (d) display the spatial ΔV maps of WSe_2/BN heterostructures with BN thicknesses of 36 nm, 45 nm, 61 nm, and 94 nm, respectively, under the illumination time of 300 s and gate voltage of Vg = -30 V during the after-writing process. Figure 4(e) shows the histograms (solid lines) of ΔV values for each BN thickness, along with Gaussian fits (dashed lines) to the data. The mean ΔV values (red circles) and the full width at half maximum (FWHM) values (black circles) as functions of BN thickness are plotted in Figure 4(f). The results indicate that ΔV increases with BN thickness, while the FWHM remains constant regardless of the BN thickness. These findings suggest that the photodoping effect, represented by ΔV, becomes more pronounced with increasing BN thickness. However, the unchanged FWHM values indicate that the inhomogeneity of photoinduced doping within BN remains unaffected by its thickness. This demonstrates that while thicker BN enhances the photodoping effect, the distribution of ΔV values, reflecting doping inhomogeneity, remains consistent. This behavior aligns with previous studies, confirming that BN thickness does not influence the spatial uniformity of photoinduced doping in WSe_2/BN heterostructures.[1-5]

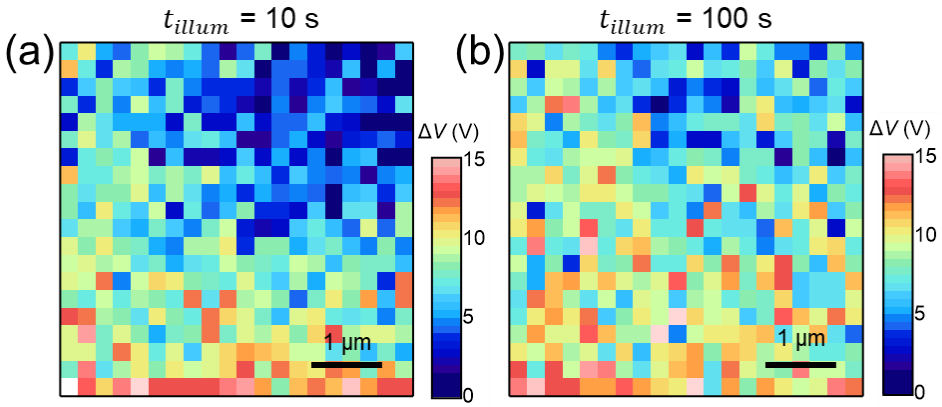

Figure 1. (a), (b) Spatially resolved ΔV images of WSe_2/BN heterostructures measured under varying t_{illum} of 10 s, 100 s.

We next investigated the dynamic behavior of the inhomogeneity of photoinduced doping in WSe_2/BN heterostructures by studying its time evolution. To achieve this, spatial ΔV maps were measured for a WSe_2/BN heterostructure with a BN thickness of 94 nm.

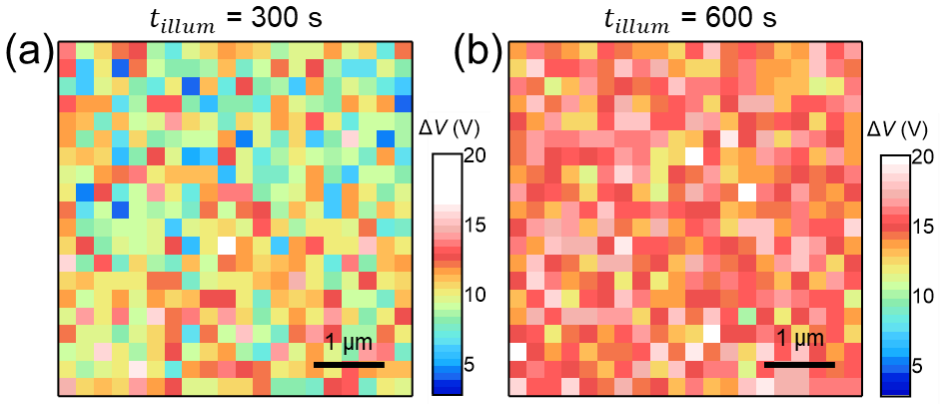

Figure 2. (a), (b) Spatially resolved ΔV images of WSe_2/BN heterostructures measured under varying t_{illum} of 300 s, and 600 s, respectively, with a gate voltage of Vg = -30 V during the after-writing process.

Measurements were conducted under the same gating electric field conditions as in Figure 1, but with varying illumination times (t_{illum}) during the after-writing process. Figures 2(a), (b) show the spatial ΔV maps for t_{illum} of 2 s, 100 s, 300 s, and 600 s, respectively. As the light exposure duration increased, a reduction in the spatial variation of ΔV, indicating decreased inhomogeneity in photoinduced doping, was observed. Figure 3 presents histograms (solid lines) of ΔV for different illumination times, overlaid by aligning their mean values. Gaussian fits (dashed lines) reveal variations in the FWHM, providing insights into the photoinduced doping patterns at the microscopic scale. Narrower FWHM values at longer t_{illum} suggest a reduction in doping inhomogeneity, attributable to changes in the photodoping environment. This behavior results from the redistribution of charged impurities within the BN substrate under varying t_{illum} conditions.

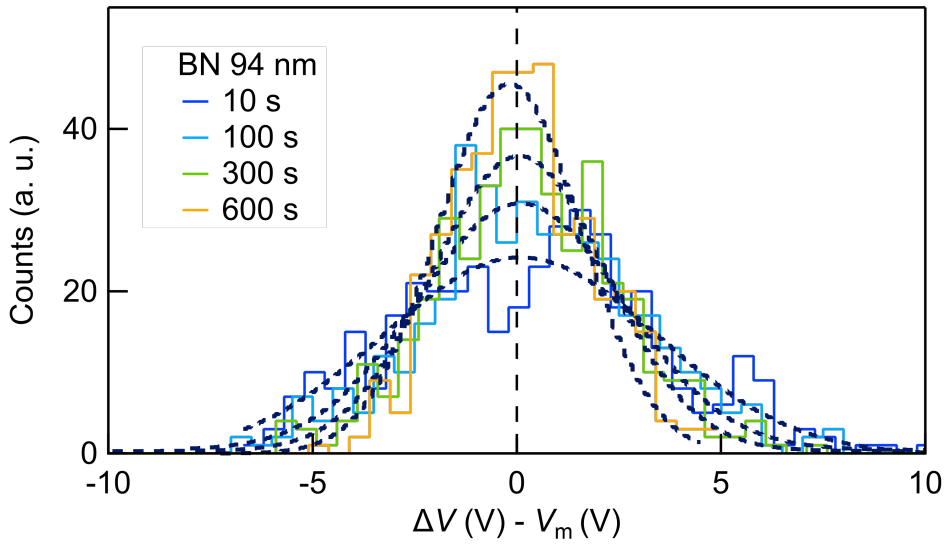

Figure 3. Histograms of ΔV for different t_{illum} where V_m are overlaid by a shift in ΔV. Dashed lines are Gaussian fits to the histograms.

Under optical illumination, electrons from donor-like defects in BN are excited into the conduction band of WSe_2 by photons, driven by the existing electric field. The ionized defects remain positively charged and localized in BN, effectively screening the back gate. For short illumination times, the migration of defect charges is insufficient, resulting in an uneven distribution of charged defects, which increases doping inhomogeneity and broadens the FWHM of the ΔV histograms. In contrast, prolonged light exposure promotes a more uniform distribution of charged defects in BN, fully screening the electric field and minimizing doping inhomogeneity, as observed in Figure 4. This reduction in inhomogeneity with extended light exposure aligns with the narrowing of the charge neutrality point (CNP) feature in transport measurements of graphene/BN heterostructures reported in earlier studies.

These studies highlight that nanoscale inhomogeneity arises from spatial disorder in BN defect density, causing transient local charge carrier fluctuations as defect charges rearrange to screen the back gate field. Figure 4 plots the FWHM as a function of t_{illum} for BN thicknesses of 36 nm, 45 nm, and 94 nm. The FWHM, indicative of doping inhomogeneity, decreases with longer t_{illum} across all BN thicknesses.

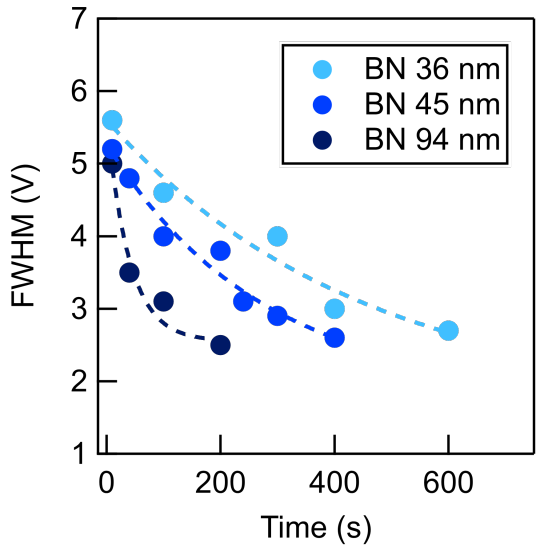

Figure 4. FWHM as a function of t_{illum} for BN thicknesses of 36 nm, 45 nm, and 94 nm. Dashed lines are polynomial fits to the data points. FWHM decreases more rapidly in thicker BN flakes.

Furthermore, the exponential fitting (dashed curves) represents that the reduction in inhomogeneity occurs more rapidly in thicker BN flakes, consistent with previous findings

that photodoping rates are higher in graphene/BN devices with thicker BN layers.[5-8]

Results and Discussion

This behavior is likely due to enhanced screening effects in thicker WSe_2 layers, which significantly diminish the influence of BN defects on ΔV. These findings align with previous studies on thickness-dependent screening properties. For this reason, we selected WSe_2 with a thickness of less than 5 nm for our WSe_2/BN heterostructure to mitigate the screening effects associated with thicker WSe_2 layers.

Acknowledgements

이 연구는 2025년 한국외국어대학교 학술연구비 지원에 의해 이루어진 것임.

References

[1] Roy, S.; Zhang, X.; Puthirath, A. B.; Meiyazhagan, A.; Bhattacharyya, S.; Rahman, M. M.; Babu, G.; Susarla, S.; Saju, S. K.; Tran, M. K.; Sassi, L. M.; Saadi, M. A. S. R.; Lai, J.; Sahin, O.; Sajadi, S. M.; Dharmarajan, B.; Salpekar, D.; Chakingal, N.; Baburaj, A.; Shuai, X.; Adumbumkulath, A.; Miller, K. A.; Gayle, J. M.; Ajnsztajn, A.; Prasankumar, T.; Harikrishnan, V. V. J.; Ojha, V.; Kannan, H.; Khater, A. Z.; Zhu, Z.; Iyengar, S. A.; Autreto, P. A. d. S.; Oliveira, E. F.; Gao, G.; Birdwell, A. G.; Neupane, M. R.; Ivanov, T. G.; Taha-Tijerina, J.; Yadav, R. M.; Arepalli, S.; Vajtai, R.; Ajayan, P. M. *Advanced Materials* **2021,** 33, (44), 2101589.

[2] Molaei, M. J.; Younas, M.; Rezakazemi, M. *ACS Applied Electronic Materials* **2021,** 3, (12), 5165-5187.

[3] Caldwell, J. D.; Aharonovich, I.; Cassabois, G.; Edgar, J. H.; Gil, B.; Basov, D. N. *Nature Reviews Materials* **2019,** 4, (8), 552-567.

[4] Rodrigues, M.-T. F.; Kalaga, K.; Gullapalli, H.; Babu, G.; Reddy, A. L. M.; Ajayan, P. M. *Advanced Energy Materials* **2016,** 6, (12), 1600218.

[5] Kumar, R.; Sahoo, S.; Joanni, E.; Singh, R. K.; Yadav, R. M.; Verma, R. K.; Singh, D. P.; Tan, W. K.; Pérez del Pino, A.; Moshkalev, S. A.; Matsuda, A. *Nano Research* **2019,** 12, (11), 2655-2694.

[6] Xie, J.; Liao, L.; Gong, Y.; Li, Y.; Shi, F.; Pei, A.; Sun, J.; Zhang, R.; Kong, B.; Subbaraman, R.; Christensen, J.; Cui, Y. *Science Advances* **2017,** 3, (11), eaao3170.

[7] Cui, X.; Lee, G.-H.; Kim, Y. D.; Arefe, G.; Huang, P. Y.; Lee, C.-H.; Chenet, D. A.; Zhang, X.; Wang, L.; Ye, F.; Pizzocchero, F.; Jessen, B. S.; Watanabe, K.; Taniguchi, T.; Muller, D. A.; Low, T.; Kim, P.; Hone, J. *Nature Nanotechnology* **2015,** 10, (6), 534-540.

[8] Chow, C. M.; Yu, H.; Jones, A. M.; Yan, J.; Mandrus, D. G.; Taniguchi, T.; Watanabe, K.; Yao, W.; Xu, X. *Nano Letters* **2017,** 17, (2), 1194-1199.

저자정보

주저자: 김태경 / 한국외국어대학교 전자물리학과 / 교수

기초과학연구 제 60 집

인쇄 2025년 8월 5일
발행 2025년 8월 8일

발 행 인 소장 허 성
운영위원 김태경, 김해조, 명희준, 이현주, 최영수
인 쇄 처 외대문화사
발 행 소 한국외국어대학교 기초과학연구소
주 소 경기도 용인시 처인구 모현읍 외대로 81
17035

ISSN 2713-7465